

Wafer-level assembly and sealing of a MEMS nanoreactor for *in situ* microscopy

L Mele¹, F Santagata¹, G Pandraud¹, B Morana¹, F D Tichelaar²,
J F Creemer¹ and P M Sarro¹

¹ DIMES-ECTM (Delft Institute of Microsystems and Nanoelectronics), Delft University of Technology, PO Box 5053, 2600 GB Delft, The Netherlands

² Delft University of Technology, Kavli Institute of Nanoscience, National Centre for HREM, Lorentzweg 1, 2628 CJ, Delft, The Netherlands

E-mail: l.mele@tudelft.nl

Received 12 March 2010, in final form 23 June 2010

Published 22 July 2010

Online at stacks.iop.org/JMM/20/085040

Abstract

This paper presents a new process for the fabrication of MEMS-based nanoreactors for *in situ* atomic-scale imaging of nanoparticles under relevant industrial conditions. The fabrication of the device is completed fully at wafer level in an ISO 5 clean room and it is based on silicon fusion bonding and thin film encapsulation for sealed lateral electrical feedthroughs. The fabrication process considerably improves the performances of previous nanoreactors. The wafer-level assembly allows faster preparation of devices, hydrocarbon contamination is no longer observed and the control of the channel height leads to a better flow reproducibility. The channel is shown to be sufficiently hermetic to work in the vacuum of a transmission electron microscope while a pressure of 100 kPa is maintained inside the nanoreactor. The transparency is demonstrated by the atomic scale imaging of YBCO nanoparticles, with a line spacing resolution of 0.19 nm.

(Some figures in this article are in colour only in the electronic version)

1. Introduction

As defined by Ehrfeld *et al* [1], microreactors are miniaturized systems fabricated by using, at least partially, methods of microtechnology and precision engineering. The advent and the further development of microreactors can have a big impact in the chemical and pharmaceutical field for the capability to combine the flexibility and versatility of batch processes and the cost-effectiveness of continuous production [2].

The miniaturization of microengineered reactors has important benefits [3–6]. First, large-scale fabrication of disposable devices is possible at low cost. A high surface–area–to–volume ratio provides excellent heat transfer and fast mass transfer, important to control potentially explosive reactions. The small volumes require less chemicals and energy and produce less waste than conventional equipment, with less risk for operator safety and environment. In the last few years, microreactors have become more and more demanding for the study of chemical processes at nanoscale [7]. Microreactors shorten the time required to transfer the

results achieved in the laboratory into production, and in fact, not only research institutes are interested in the development of microfabricated chemical systems but also industry [8].

Finally, small reactor sizes enable integration into analysis equipment. Recently, a nanoreactor has been developed that fits into transmission electron microscopes (TEM) and scanning transmission x-ray microscopes [9–11]. The MEMS-based nanoreactor is a research device that is very thin and transparent enough to enable the live imaging of nanoparticles in TEM at 100 kPa and 500 °C with atomic scale resolution. The device opens new perspectives in the study of particles at the atomic level.

However, the MEMS nanoreactor [12] has a number of drawbacks that are related to the method of fabrication.

First, the reactor assembly and sealing are extremely time consuming and dominate the production time. This is highly undesirable because the reactor is meant to be a batch fabricated, disposable device. The reason behind this is that the alignment and sealing is done manually and separately for each reactor.

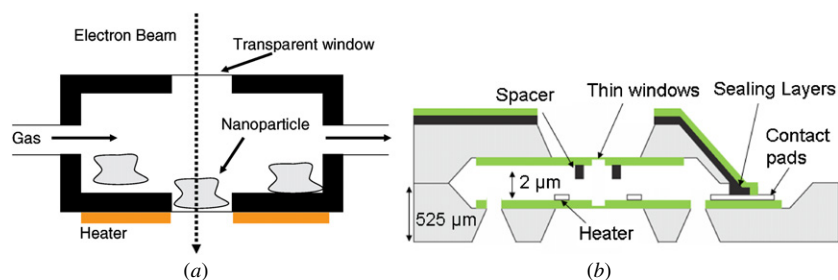


Figure 1. Schematic layout of a windowed cell (a) and schematic cross-section of the wafer-bonded nanoreactor (b).

Second, the reactors often suffer from contamination by hydrocarbons. Hydrocarbon molecules are released by the employed epoxy adhesive when it is not entirely cross-linked. The molecules are cracked when they come in contact with the electron beam of an electron microscope. As a consequence, they deposit as black carbon on the reactor window and on the nanostructured material under investigation. This obscures the images and, more importantly, interferes with the chemical surface reactions under study.

Finally, the reactors have a flow resistance that varies up to a factor of 100 below the calculated value [11] due to the presence of particles between the two dies [13]. For the study of some types of reactions this is an undesirable situation. A high level of cleanliness is therefore required during assembly.

To solve the aforementioned problems, a novel method for the assembly and sealing of the nanoreactors has been developed. The method is based on the combination of silicon fusion bonding and thin-film encapsulation of electrical feedthroughs. Wafer bonding and encapsulation are wafer-level operations and thus are much faster than the original die-by-die approach. Both techniques can be employed without using hydrocarbons. The fusion bonding and encapsulation were integrated into the original fabrication process [9], which therefore had to be modified considerably. The novel process preserves the main features of the original reactor, such as the dimensions, the hermeticity in a high vacuum environment, the maximum operating pressure of 100 kPa and the unrivalled atomic-scale transparency.

This paper starts with a brief description of the reactor principle. Then, it discusses the novel manufacturing method, with a focus on wafer bonding, thin-film sealing and process integration. The novel reactors are characterized in experiments using AFM (atomic force microscopy), optical microscopy, infrared imaging, TEM and RGA (residual gas analysis).

The results demonstrate that the proposed method has indeed significantly reduced the fabrication time of the nanoreactors, has removed hydrocarbon contamination and the uncertainty in the channel height, while preserving both hermeticity and atomic-scale transparency.

2. Design

The nanoreactor has been designed in order to provide atomic-scale resolution of nanostructured materials in gas or liquid environment with working conditions of 100 kPa and 500 °C.

The device is a membrane-type nanoreactor based on the windowed cell concept [9–11]. In *in situ* TEM investigation, the sample is continuously exposed to the reactive gas or liquid [12]. The environment is confined in a closed cell with outside connections for the loading and the collection of the gas or liquid (figure 1(a)). Imaging at the atomic scale is possible provided that the scattering along the electron beam path is minimized. This can be achieved by reducing the thickness of the cell and by embedding thin electron transparent windows. The presence of a heating system enables the temperature control inside the cell.

The reactor is fit into a dedicated specimen holder to position it into the microscope and to connect it with an external gas supply system and a temperature controller [11]. Gas sealing is done with Viton O-rings, which are commonly applied in high vacuum systems.

In figure 1(b) it is shown how the windowed cell concept has been converted into a MEMS nanoreactor, assembled by wafer-level fusion bonding and sealed lateral electrical feedthroughs by the deposition of a non-conformal layer. The device footprint is $10 \times 3.3 \text{ mm}^2$ and it has a narrow channel connecting inlet and outlet. The channel is about $2 \mu\text{m}$ high and it is formed by etching a $3 \mu\text{m}$ deep recess into the silicon on both halves. In the middle of the channel a $1 \times 1 \text{ mm}^2$ free-standing membrane is released to form the reaction chamber and ensure good thermal insulation. The membranes are made of low stress LPCVD SiN [14] and their thickness is $1 \mu\text{m}$ in order to stand the stress arising from the bulging at a pressure difference of 100 kPa which locally increases the height of the channel up to $35 \mu\text{m}$ [11]. On the top half, an array of LPCVD TEOS spacers is made in order to prevent the stiction of the two membranes. To allow high resolution TEM (HRTEM), the reaction chamber is fabricated with 20 electron transparent windows made of 15 nm thick LPCVD silicon nitride. They have a $20 \mu\text{m} \times 6 \mu\text{m}$ elliptical shape and on the top half the windows are rotated by 90° with respect to the bottom half in order to facilitate their alignment during the bonding.

The heater is a thin-film resistor spiral embedded on the bottom membrane. Four contact pads enable the control and the sensing of the temperature after calibration of the resistance. The heater is made of platinum (Pt) deposited on top of the tantalum (Ta) layer. The combination of these two materials provides good adhesion up to 550 °C and a reversible resistance change [15].

The channel will be defined as hermetic for our purposes if leaks into the microscope vacuum have negligible effects

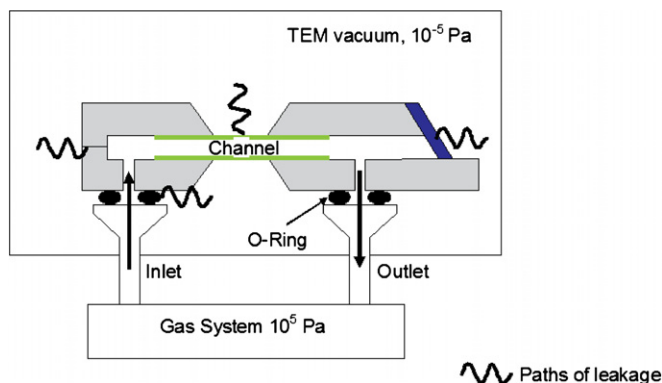


Figure 2. Block diagram of the nanoreactor connected to the gas system and loaded in the TEM indicating possible paths of leakage.

on the vacuum pressure. In fact, when the nanoreactor is connected to the gas supply through the TEM specimen holder, the device and the gas supply can be seen as a single closed system (figure 2). During the operation a pressure of 100 kPa is present inside the channel, while the device is surrounded by the high vacuum (10^{-5} Pa) of the TEM chamber. The possible paths of leakage are the 15 nm thick windows, the connections between inlet/outlet and the gas system and the sidewalls of the channel.

3. Fabrication

3.1. Fusion bonding of the channel

Most of the wafer bonding techniques cannot be applied to the TEM nanoreactor. Adhesive bonding with epoxy may cause hydrocarbon contamination because of outgassing. Anodic bonding is not suited because the use of glass would complicate the machining required for the realization of thin electron transparent windows. Eutectic bonding cannot be applied because the presence of the metal alloy can interfere with the catalytic reaction. Silicon fusion bonding is the best candidate for the assembly of the TEM nanoreactors. In fact, both halves can be finely machined and no intermediate layers that could interfere with the device performances are required. Silicon fusion bonding [16–18] is achieved by the spontaneous joining of two silicon surfaces provided that their RMS roughness is lower than 0.5 nm [19, 20] and high cleanliness is ensured. A particle between the two mating surfaces causes an unbonded area with radius R that is up to four orders of magnitude larger than the radius h of the particle itself [21]. Below a certain value h_{crit} , the radius of the unbonded area is practically equal to the size of the particle. The typical value of h_{crit} is around 0.1 μm . Particles larger than h_{crit} must be removed before bonding in order to have leak-tight reactors.

The prime surface of a new silicon wafer already fulfils the requirements for a reliable fusion bonding in terms of roughness and cleanliness. To preserve its initial quality, the surface was covered by a protective layer during the full processing (wrapping) and removed only prior to bonding (unwrapping). This protective layer should not roughen the silicon surface during deposition and subsequent removal.

Thermal oxide was chosen for two reasons: thermally grown SiO_2 hardly affects the silicon roughness [22] and it can be removed in buffered hydrofluoric acid (BHF) without etching the silicon surface [23].

After unwrapping, the silicon surfaces are properly activated and cleaned from particles and organics in an RCA-1 solution [24]. The solution is composed of water, hydrogen peroxide and ammonia at a 5:1:1 ratio heated up to 75 $^{\circ}\text{C}$. Besides highly clean wafers, the RCA-1 gives hydrophilic surfaces with a large density of dangling OH groups. The surfaces are thus highly activated and they bond by forming hydrogen bridges when brought into close contact, even at room temperature.

The wafers are bonded in ambient air and then annealed for 1 h at 500 $^{\circ}\text{C}$, with a temperature ramp up of 10 $^{\circ}\text{C min}^{-1}$. A further strengthening of the bond is achieved during the LPCVD SiN deposition at 850 $^{\circ}\text{C}$ performed later in the fabrication process.

The control of the surface roughness and the size of particles ensures good adhesion between the two bonded surfaces and therefore an improved control of the channel height.

3.2. Electrical feedthroughs

Electrical feedthroughs are needed to provide electrical connections to the internal heater (figure 1(b)). Electrical feedthroughs in hermetic cavities are always challenging. Two possible configurations are vertical and lateral feedthroughs [25, 26], but for the TEM nanoreactor the latter ones are more adequate. Lateral electrical feedthroughs allow the contact pads to be placed in the desired position and make use of standard batch fabrication steps. Various solutions are summarized in [26]. The use of interfacial materials with low melting point is not compatible with high vacuum and reaction gases, while highly doped regions in the silicon show a high resistance that limits the current that can flow through the heater and cause surface roughening. In the solution proposed here the heater and its contact pads are patterned in a 3 μm deep recess and made accessible through a via on the top wafer. Therefore a lateral gap on the side of the feedthroughs leaves the channel open once the two halves are bonded together. The gap is closed by the deposition of a non-conformal layer to prevent deposition inside the cavity. The sealing material is PECVD TEOS deposited at 350 $^{\circ}\text{C}$. The deposition rate on the bottom of the 525 μm deep cavity of the lid wafer has been measured to be 15% lower than the value measured on a plain test wafer. Therefore, 4 μm PECVD TEOS has been deposited to seal the channel completely. The PECVD TEOS is later covered with 500 nm low stress LPCVD SiN. The layer acts as hard mask for KOH etch and the high temperature eliminates any remaining organic molecules. Moreover, the LPCVD SiN provides further hermeticity to the sealing.

3.3. Bottom and top wafer processing

The starting material is a 100 mm single side polished silicon wafer, with (100) crystal orientation and a thickness of

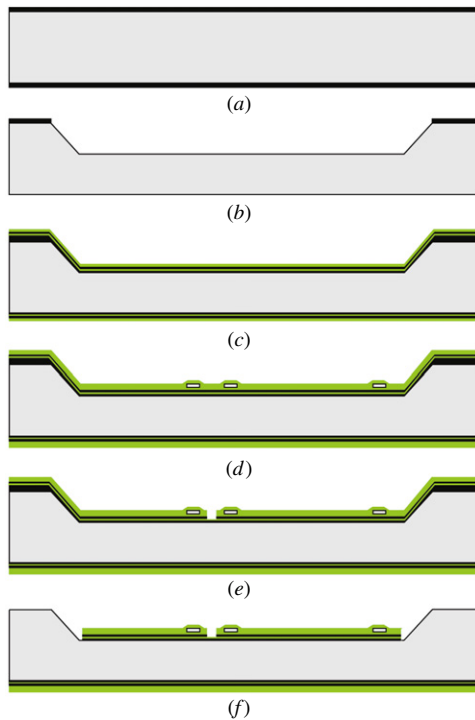


Figure 3. Process flow for the bottom wafer. (a) protective oxide (wrapping), (b) recess opening, (c) LPCVD depositions, (d) heater, (e) opening of electron transparent windows, (f) removal of the stack of layers on the bonding area (unwrapping).

525 μm . The process is described separately for bottom and top dies.

The fabrication steps for the bottom dies are shown in figure 3. First, a 300 nm thermal oxide layer is grown to act as protective layer (figure 3(a)). The oxide is patterned in buffered hydrofluoric acid (BHF) to define the geometry of the channel. Then a 3 μm deep recess is open in the silicon by deep reactive ion etching (DRIE) (figure 3(b)). The etching is tuned in order to have slanted sidewalls (about 45 °C) and smooth edges that improve the uniformity of the photoresist spinning in the following lithography steps. The recess forms the channel of the nanoreactor. Next, 200 nm thermal oxide is grown to improve the adhesion of the 15 nm low stress LPCVD silicon nitride for the electron transparent windows. The layers are covered first with 400 nm LPCVD TEOS, used as a stop layer for windows opening, and then with 500 nm low stress LPCVD silicon nitride to form a large membrane (figure 3(c)). The heater is patterned by a lift-off process (figure 3(d)) and covered by 500 nm low stress LPCVD silicon nitride afterward. Next, electron transparent windows are opened on the front side by dry etching of the nitride and further wet etching in BHF of the 400 nm LPCVD TEOS is done to stop on the thin silicon nitride layer (figure 3(e)).

Once all the components of the channel are fabricated, the bare silicon has to be unwrapped over the bonding surface. For this purpose, the stack of layers is dry etched down to the protective thermal oxide which is then stripped in BHF (figure 3(f)). The effectiveness of this approach is discussed in section 5.

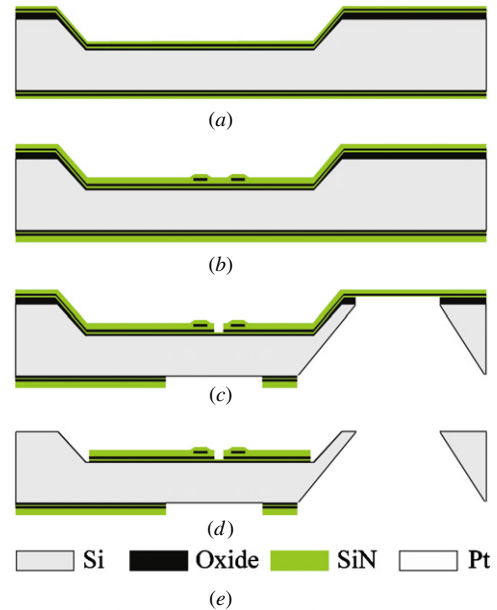


Figure 4. Process flow for the top wafer. (a) protective oxide (wrapping) + recess opening + LPCVD depositions, (b) spacers, (c) through wafer hole for the access to the contact pads + opening of electron transparent windows, (d) removal of the stack of layers on the bonding area (unwrapping).

The top wafer (figure 4(a)) follows the same process flow as the bottom one until the step described in figure 3(c). On top of the 500 nm LPCVD silicon nitride, the spacers (figure 1(b)) are patterned by deposition of 1 μm thick LPCVD TEOS and wet etching in BHF. Next, a deposition of 500 nm low stress LPCVD silicon nitride is done in order to form the 1 μm thick membrane. A via hole is opened through the entire wafer from the back-side in wt%33 KOH at 85 °C in order to allow the access to the contact pads after bonding. The back-side is also patterned by etching the stack of layers down to the silicon for the release of the LPCVD SiN membrane in the KOH etching performed after bonding (figure 4(c)). Next, the opening of the electron transparent windows and the unwrapping are performed as already explained in figures 3(e), (f) for the bottom wafer (figure 4(d)).

3.4. Bonding and post-bonding processing

The wafers are cleaned in RCA-1 and then aligned on the EV 420 contact aligner that provides an accuracy of 2 μm , which is sufficient to ensure the overlay of the electron transparent windows. The aligned wafers are transferred in an EV 501 bonder where they are bonded and annealed. After bonding the channel is opened on the side of the electrical feedthrough (figure 5(a)) and it is closed by depositing 4 μm of PECVD TEOS at 350 °C (figure 5(b)), with a pressure inside the cavity of about 3 mbar. The sealing layer is then covered by 500 nm LPCVD silicon nitride. The two faces of the bonded wafers are patterned for KOH etching (figure 5(b)). After wt%33 KOH at 85 °C (figure 5(c)), the reaction chamber and inlet/outlet of the channel are defined. The etching stops on the thermal oxide that is left to protect the electron transparent windows in the following steps. Next, contact pads

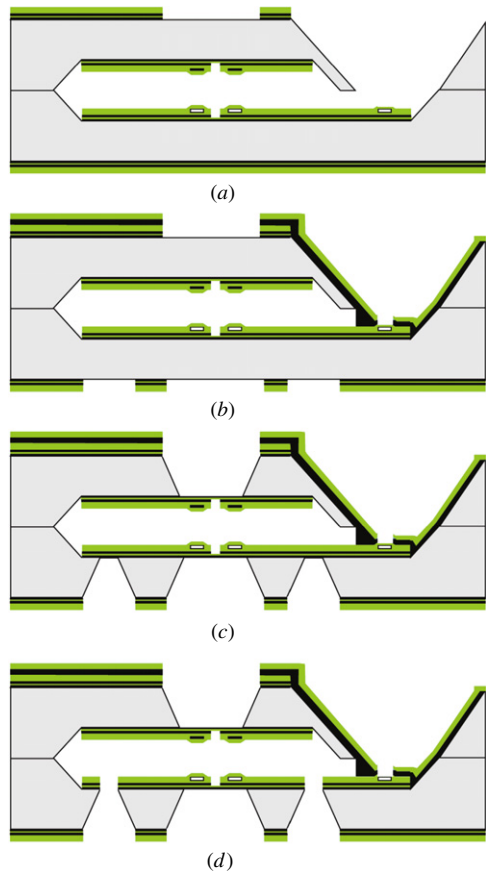


Figure 5. Process flow after bonding. (a) bonding (channel open), (b) sealing + KOH patterning, (c) KOH etching, (d) contact pads and inlet/outlet.

are opened (figure 5(d)) with the aid of a silicon wafer shadow mask fabricated by DRIE. The wafer is diced in $10 \times 3.3 \text{ mm}^2$ dies. Another shadow mask is used for the opening of inlet and outlet in a fluorine based etcher. The cross section of the final reactor is depicted in figure 5(d).

4. Experiments

The quality of the bonding process was tested with atomic force microscopy (AFM), particle counting and infrared inspection. AFM measurements were performed on a silicon new wafer and on the processed surfaces prior to bonding, after the removal of the protective oxide to check the variation of surface roughness. Measurements were carried out on the NT-MDT nTegra Maximus with a scan size of $0.5 \times 0.5 \mu\text{m}^2$, resolution of 512×512 points and scanning frequency of 2 Hz. The comparison between the two AFM profiles is given by the computation of the power spectral density (PSD). Then the number and the size of particles over the bonding surface were investigated on a Nanophotonics Reflex TT Particle Counter that has particle sensitivity down to 90 nm. As described in [21], particles larger than $0.1 \mu\text{m}$ give voids larger than $1000 \mu\text{m}$. Because the smallest bondframe width of the nanoreactor is $400 \mu\text{m}$, all particles that are much larger than $0.1 \mu\text{m}$ can potentially cause leaks. Voids were detected by infrared inspection, using a NET FOculus B/W Camera,

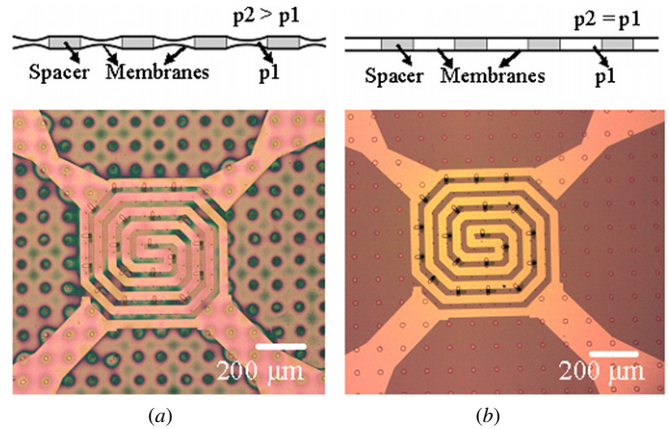


Figure 6. Optical leak test. When the channel is closed the two membranes are pressed together because of the pressure difference causing fringes of optical interference (a). The opening of the channel and/or leakage cause the straightening of the membranes (b).

$2/3''$ progressive scan Ex-View CCD (ICX285) SXGA 1392×1040 , equipped with a Fujinon 12.5 mm /F1.4–16 lens with 850 nm infrared long-pass filter. Defects on the surface or the presence of particles lead to unbonded areas that appear as interference fringes [27].

The yield is evaluated by counting how many devices are still bonded and hermetically closed after dicing. To check the hermeticity, a first inspection is done under an optical microscope. After the sealing by the PECVD TEOS deposition the channel is closed with an inside pressure of around 3 mbar (figure 5(d)) until inlet and outlet are opened. Because of the pressure difference with the outside atmosphere, the central membranes are pressed together. The effect appears as a pattern of interference fringes under an optical microscope (figure 6(a)). The presence of a leakage or the opening of inlet/outlet causes a pressure increase inside the channel and fringes disappear when the inside pressure becomes 1 bar (figure 6(b)).

This is a means to quickly check whether the devices are hermetically sealed. Further proof was given by residual gas analysis (RGA) on two nanoreactors with the inlet/outlet still closed. Source gases for PECVD TEOS deposition are TEOS, C_2F_6 and O_2 . Therefore, assuming that right after the sealing no N_2 is trapped inside the channel, the detected partial pressure of nitrogen is indicative of air flow through potential leakage paths.

The leak rate r_{leak} can be calculated according to

$$r_{\text{leak}} = \frac{\Delta p \cdot V}{t}, \quad (1)$$

where V is the volume of the channel in liters, Δp is the N_2 partial pressure in mbar and t is the time passed since sealing. The uncertainty of the measurement is 10% for He, Ar, CO_2 , H_2O and O_2 and 5% for N_2 and H_2 .

The final test of hermeticity was the insertion of the nanoreactor in the TEM Philips CM300UT-FEG: the device was first loaded in the dedicated specimen holder, and then the inlet was backfilled at a pressure of 100 kPa. The

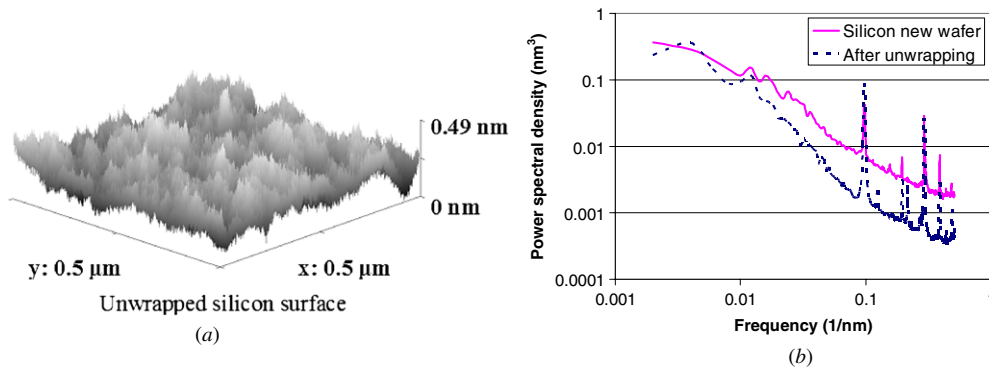


Figure 7. AFM measurement on the silicon surface after the removal of the protective oxide (a). The scan size is $0.5 \times 0.5 \mu\text{m}^2$ with a resolution of 512×512 points. The RMS roughness of 0.09 nm. In figure 7(b), the power spectral density (PSD) analysis shows that the RMS roughness of the silicon surface after unwrapping is slightly decreased.

pressure rise in the microscope column (nominally 10^{-5} Pa) was monitored.

The flow rate strongly depends on the channel height h ($\propto h^{-3}$) and therefore the flow reproducibility was deduced from the variation in channel height, estimated from the full wafer infrared inspection. The presence of particles trapped between the two wafers in proximity of the channel causes the increase of the height h . As described in [28], if Newton’s rings are not observed in the infrared image of the bonded wafers, only gaps much smaller than $0.5 \mu\text{m}$ can be present. Since for the nanoreactor h is equal to $2 \mu\text{m}$, the maximum variation of the channel height for hermetically bonded nanoreactors is much smaller than 25% and therefore the maximum flow variation is expected to be much smaller than a factor 2 (1.25^3).

Electrical feedthroughs were inspected under a scanning electron microscope (SEM), to observe whether the channel was sealed by the PECVD TEOS deposition. The TCR of the heater was measured in the temperature range from 0°C to 200°C on a Cascade probe station with a heated chuck and an HP 4146C parameter analyzer.

Finally, the cleanliness from hydrocarbons and the atomic-scale transparency were tested in a TEM, a Philips CM300UT-FEG. The point resolution limit of the TEM is 0.17 nm. By exposing the windows to the electron beam, the presence of hydrocarbon contamination would appear as a dark ring as a consequence of decomposition in the e-beam and the deposition of the carbon as soot. Nanoparticles of yttrium barium copper oxide (YBCO) were loaded in the nanoreactor by making a suspension with ethanol. After loading, the ethanol evaporates leaving nanoparticles all over the channel and the windows. Particles deposited on the thin transparent windows were imaged by inserting the nanoreactor in the TEM vacuum column. The TEM image was then analyzed with ImageJ [29] to calculate the 2D Fast Fourier transform (FFT) and identify the minimum lattice distance that can be resolved.

5. Results and discussion

The RMS roughness measured on a new silicon wafer is 0.10 nm. In figure 7(a) the AFM measurement on the silicon surface after the unwrapping step described in figure 3(f) is

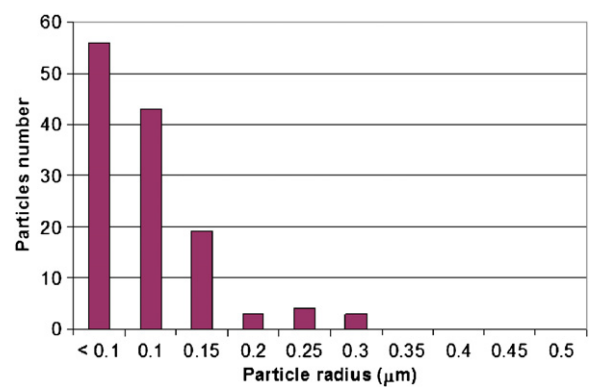


Figure 8. Particle counting on the bonding surface after RCA-1 cleaning. Particles bigger than $0.1 \mu\text{m}$ are mainly located on the edges.

reported. The RMS roughness for this surface is 0.09 nm that is slightly smaller than the value measured on a new silicon wafer. Figure 7(b) shows the PSDs calculated from the AFM measurements. The area under the two profiles represents the RMS roughness for the corresponding surface. As can be seen the two spectra are comparable over the full range of frequency. Few peaks are observed for the two measurements at the same frequencies and probably they are caused by the noise generated by floor vibrations. The results of the surface morphology show therefore the effectiveness of the silicon oxide as a protective layer for the bonding surface.

In figure 8(a) summary of the particles measured on the wafer after the cleaning in RCA-1 is reported. Most of the particles are smaller than the critical value of $0.1 \mu\text{m}$ or comparable with it. Particles that are twice as large as $0.1 \mu\text{m}$ are mainly detected on the outer region of the wafer (not shown here) and therefore they do not affect the hermetic bonding of the devices. Evidence of the quality of the bonding is given by the inspection of the bonded wafer on an infrared setup (figure 9). As can be seen, some defects due to surface imperfection or particles appear as interference fringes and they are located near the edges of the wafer, but the majority of the area is intact.

After dicing all the devices are still bonded together and under the optical microscope the pattern of interference

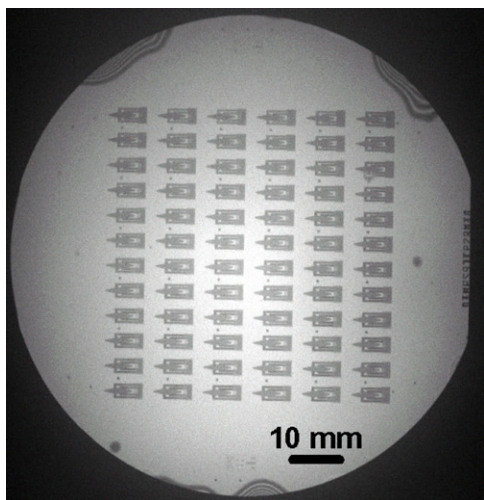


Figure 9. Infrared image of bonded wafers. No voids are detected.

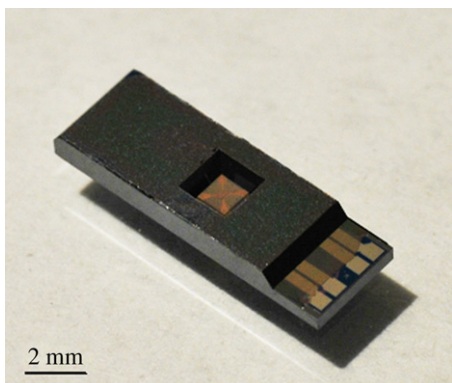


Figure 10. Photograph of the nanoreactor after dicing.

fringes on the membranes (figure 6) is observed on 90% of the nanoreactors. This means that only the remaining 10% is not hermetic due to either the failure of some window or the presence of some leakage path. The final device after dicing is shown in figure 10.

The new wafer-level assembly process leads to a faster fabrication speed. In fact the full assembly procedure including the wafer bonding, annealing, and thin-film sealing lasts around 8 h, which gives a reduction of almost 95% in time compared to the procedure for assembly with adhesive of single dies.

The gas composition measured with RGA in two representative nanoreactors with channel closed is given in table 1. The time elapsed between the end of the processing and the test was 5 months and fringes were still visible on these samples as shown in figure 6(a).

In the two samples the total pressure was higher than the pressure during PECVD TEOS deposition (3 mbar). In sample 1 the main gas is H₂. This is one of the primary outgassing species from PECVD TEOS [30]. Outgassing is probably promoted by the high temperature reached during the following LPCVD SiN deposition. The partial pressure of N₂ is 3.87 mbar that gives a leak rate of 3.28×10^{-15} mbar·l s⁻¹ by applying equation (1). In sample 2 the presence

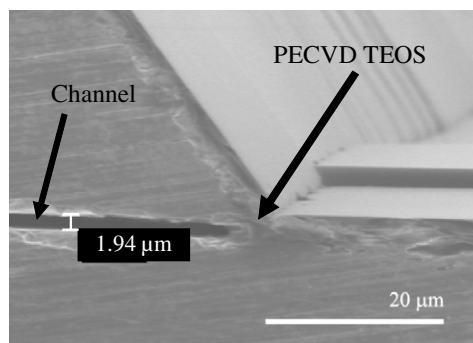


Figure 11. SEM image showing the thin-film sealing of the channel by PECVD TEOS.

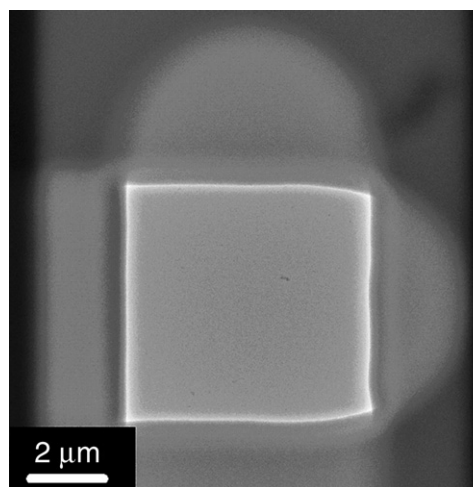


Figure 12. TEM image of two superimposed windows with alignment within specifications.

Table 1. Gas composition measured with RGA on two nanoreactors 5 months after bonding: nitrogen is representative of the air that flows inside the channel through paths of leakage. Leak rate of 3.28×10^{-15} mbar·l/s and 1.64×10^{-13} mbar l s⁻¹ are measured respectively for samples 1 and 2.

	Sample 1		Sample 2	
	mbar	%	mbar	%
H ₂	23.60	84.65	17.30	7.83
He	0.02	0.05	0.02	0.01
N ₂	3.87	13.88	194.00	87.80
H ₂ O	0.32	1.13	0.64	0.29
O ₂	0.00	0.00	3.29	1.49
Ar	0.00	0.00	5.45	2.47
CO ₂	0.08	0.29	0.26	0.12
Tot	27.88	100.00	220.96	100.00

of N₂ is predominant, while the H₂ partial pressure is comparable with the measurement on sample 1. This device shows a higher leakage with respect to sample 1 that is 1.64×10^{-13} mbar l s⁻¹ which is however still small. The final test of the hermeticity is the loading of the nanoreactors in the TEM. For these devices, the leakage measured in the microscope reached a negligible low constant value which does not affect the vacuum level in the column of the TEM.

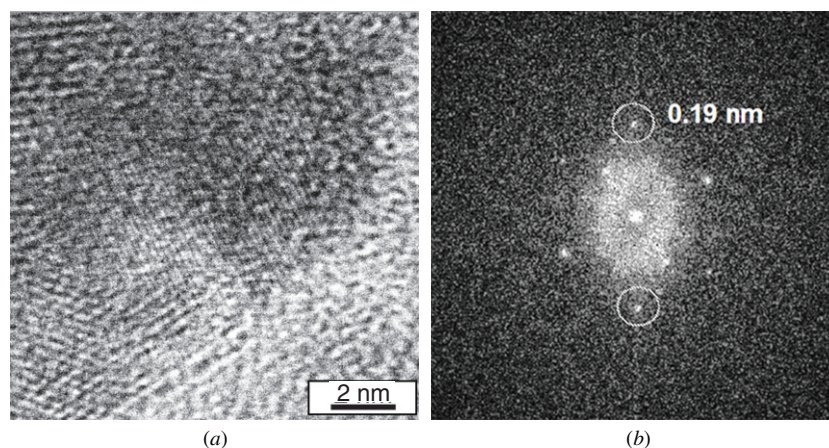


Figure 13. Atomic-scale TEM image of a nanoparticle of yttrium barium copper oxide: (a) and 2D fast Fourier transform; (b) the minimum resolved lattice space is 0.19 nm.

The SEM image in figure 11 shows the thin film encapsulation for the lateral electrical feedthroughs. The gap where the feedthroughs are made is completely closed by the PECVD TEOS, thus sealing the channel. The heater exhibits a resistance of $166 \pm 3 \Omega$ at room temperature, with a temperature coefficient of resistance (TCR) of $1.89 \times 10^{-3} \text{ K}^{-1}$.

Next, flow rate uniformity was estimated. As can be seen in figure 9, no interference fringes are observed in the devices footprint. As explained in section 4, this implies that the flow variation from device to device is probably much smaller than a factor 2 over the full wafer. This is a considerable improvement with respect to the adhesive-based nanoreactor in which the flow rate can change up to a factor 100 from device to device. The better flow reproducibility is a direct consequence of the new fabrication method, in which the fine control of the surface roughness and cleanliness is required for the achievement of hermetic silicon fusion bonding.

Finally, the nanoreactor was tested in the TEM for the imaging of nanoparticles. Figure 12 shows a TEM image of two superimposed windows that are aligned within specification. None of the tested windows experienced hydrocarbon contamination above the nominal background level. This is the main improvement with respect to the previous nanoreactor where the outgassing of the epoxy adhesive may considerably interfere with the operation.

In figure 13(a) the lattice fringes of YBCO nanoparticles can be seen in the upper-left corner, while the windows appear as an amorphous layer in the bottom-right corner. The 2D Fast Fourier transform is calculated in figure 13(b). The wave vector corresponding to the minimum periodic spacing that is resolved is highlighted by circles. The maximum line spacing resolution is 0.19 nm, proving that HRTEM imaging can be successfully achieved with this wafer-bonded nanoreactor.

6. Conclusions

The wafer-bonded MEMS nanoreactor represents a considerable improvement of the previous version assembled

by adhesive. In fact, all the main features are preserved, such as hermeticity and atomic-scale resolution in TEM, but fabrication speed, flow reproducibility and cleanliness are much improved. The new fabrication allows the successful bonding of 90% of the devices at wafer level all at once, with a reduction in time of 95% with respect to the assembly by adhesive. The flow variations reduced from a factor 100 to well below a factor 2, due to the fine control of surface roughness and particles size needed for the silicon fusion bonding. Finally, the nanoreactor is free from hydrocarbon contamination.

This improved fabrication process opens up the way for a rapid reproduction of nanoreactors with a constant quality. This will stimulate their use as a powerful tool for the understanding of chemical processes at nanoscale.

Acknowledgments

The authors would like to thank the DIMES IC processing group, especially Johan van der Cingel for AFM measurements, Charles de Boer for help in the optimization of the PECVD TEOS deposition, and Jan Groeneweg for RCA-1 cleaning and Loek Steenweg for dicing. This work was performed in the framework of NIMIC (Nano IMaging under Industrial Conditions), a SmartMix project of the Ministry of Economic Affairs.

References

- [1] Ehrfeld W, Hessel V and Löwe H 2000 *Microreactors: New Technology for Modern Chemistry* (Weinheim: Wiley-VCH)
- [2] Roberge D M, Ducry L, Bieler N, Cretton P and Zimmermann B 2005 Microreactor technology: a revolution for the fine chemical and pharmaceutical industries? *Chem. Eng. Technol.* **28** 318–23
- [3] Löwe H and Ehrfeld W 1999 State-of-the-art in microreaction technology: concepts, manufacturing and applications *Electrochim. Acta* **44** 3679–89
- [4] Gavrilidis A, Angeli P, Cao E, Yeong K K and Wan Y S S 2002 Technology and applications of microengineered reactors *Chem. Eng. Res. Des.* **80** 3–30

- [5] Wörz O, Jäckel K P, Richtert T and Wolf A 2001 Microreactors, a new efficient tool for optimum reactor design *Chem. Eng. Sci.* **56** 1029–33
- [6] Quiram D J, Hsing I-M, Franz A J, Jensen K F and Schmidt M A 2000 Design issues for membrane-based, gas phase microchemical systems *Chem. Eng. Sci.* **55** 3065–75
- [7] Jensen K J 2001 Microreactor engineering—is small better? *Chem. Eng. Sci.* **56** 293–303
- [8] Zhang X, Stefanick S and Villani F J 2004 Application of microreactor technology in process development *Org. Process Res. Dev.* **8** 455–60
- [9] Creemer J F, Helveg S, Hoveling G H, Ullmann S, Kooyman P J, Molenbroek A M, Zandbergen H W and Sarro P M 2009 MEMS nanoreactor for atomic-resolution microscopy of nanomaterials in their working state *Proc. IEEE. Conf. MEMS (Sorrento, Italy, 2009)* pp 76–9
- [10] Creemer J F, Helveg S, Hoveling G H, Ullmann S, Molenbroek A M, Sarro P M and Zandbergen H W 2008 Atomic-scale electron microscopy at ambient pressure *Ultramicroscopy* **108** 993–8
- [11] Creemer J F, Helveg S, Kooyman P J, Molenbroek A M, Zandbergen H W and Sarro P M 2010 A MEMS reactor for atomic-scale microscopy of nanomaterials under industrially relevant conditions *J. Microelectromech. Syst.* **19** 254–64
- [12] Sharma R 2005 An environmental transmission electron microscope for *in situ* synthesis and characterization of nanomaterials *J. Mater. Res.* **20** 1695–707
- [13] Robertson J K and Wise K D 2001 Modeling a microfluidic system using Knudsen's empirical equation for flow in the transition regime *J. Vac. Sci. Technol. A* **19** 358–64
- [14] French P J, Sarro P M, Mallee R, Fakkeldij E J M and Wolffenbuttel R F 1997 Optimization of a low-stress silicon nitride process for surface-micromachining applications *Sensors Actuators A* **58** 149–57
- [15] Tiggelaar R Silicon-technology based microreactors for high-temperature heterogeneous partial oxidation reactions *PhD Thesis* University of Twente, Enschede, The Netherlands
- [16] Alexe M and Gösele U 2004 *Wafer Bonding: Applications and Technology* (Berlin: Springer)
- [17] Zhang X X and Raskin J-P 2005 Low-temperature wafer bonding: a study of void formation and influence on bonding strength *J. Microelectromech. Syst.* **14** 368–82
- [18] Berthold A and Vellekoop M J 1997 IC-compatible silicon wafer-to-wafer bonding *Sensors Actuators A* **60** 208–11
- [19] Gui C, Jansen H, de Boer M, Berenschot J W, Gardeniers J G E and Elwenspoek M 1997 High aspect ratio single crystalline silicon microstructures fabricated with multi layer substrates *Proc. Transducers'97 (Chicago)* pp 633–6
- [20] Wiegand M, Reiche M, Gösele U, Gutjahr K, Stolze D, Longwitz R and Hiller E 2000 Wafer bonding of silicon wafers covered with various surface layers *Sensors Actuators* **86** 91–5
- [21] Tong Q Y and Gösele U 1994 Semiconductor wafer bonding: recent developments *Mater. Chem. Phys.* **37** 101–27
- [22] Liu Q, Spanos L, Zhao C and Irene E A 1995 A morphology study of the thermal oxidation of rough silicon surfaces *J. Vac. Sci. Technol. A* **13** 1977–83
- [23] Williams K R, Gupta K and Wasilik M 2003 Etch rates for micromachining processing—part II *J. Micromech. Syst.* **12** 761–78
- [24] Reinhardt K A and Kern W 2008 *Handbook of Silicon Wafer Cleaning Technology* (Norwich: William Andrew)
- [25] Burger G J, Smulders E J T, Berenschot J W, Lammerink T S J, Fluitman J H and Imai S 1996 High-resolution shadow-mask patterning in deep holes and its application to an electrical feed-through *Sensors Actuators A* **54** 669–73
- [26] Esashi M 2008 Wafer level packaging of MEMS *J. Micromech. Microeng.* **18** 1–13
- [27] Bollmann D, Landesberger C, Ramm P and Habberger K 1996 Analysis of wafer bonding by infrared transmission *J. Appl. Phys.* **35** 3807–9
- [28] Harendt C, Graf H-G, Penteker E and Hofflinger B 1990 Wafer bonding: investigation and *in situ* observation of the bond process *Sensors Actuators* **A21–A23** 927–30
- [29] Abramoff M D, Magelhaes P J and Ram S J 2004 Image processing with ImageJ *Biophotonics Int.* **11** 36–42
- [30] Hirashita N, Tokitoh S and Uchida H 1993 Thermal desorption and infrared studies of plasma-enhanced chemical vapor deposited SiO films with tetraethylorthosilicate *Japan. J. Appl. Phys.* **32** 1787–93